Materials Science & Engineering A 765 (2019) 138289

Contents lists available at ScienceDirect

Materials Science & Engineering A

journal homepage: www.elsevier.com/locate/msea

Mechanical performance and microstructural characterisation of titanium alloy-alloy composites built by wire-arc additive manufacture

A.E. Davis[a,*], C.I. Breheny[a], J. Fellowes[b], U. Nwankpa[c], F. Martina[c], J. Ding[c], T. Machry[d], P.B. Prangnell[a]

[a] School of Materials, University of Manchester, M13 9PL, UK
[b] School of Earth and Environmental Sciences, University of Manchester, M13 9PL, UK
[c] Welding Engineering and Laser Processing Centre, Cranfield University, Bedfordshire, MK43 0PL, UK
[d] Formerly at Airbus Operations, Now at Satair, Airbus SAS, Weg beim Jaeger 150, 22335, Hamburg, Germany

ARTICLE INFO

Keywords:
Titanium alloys
Additive manufacturing
Characterization
Grains and interfaces
Mechanical properties
Fracture behaviour

ABSTRACT

A first stage study has been performed to investigate the potential for exploiting high deposition rate WAAM to print dual-alloy microstructures. Samples were built using alternating feed wires of commercially-pure Ti and Ti–6Al–4V. A high level of dilution occurred during deposition accompanied by effective liquid-phase mixing, producing a regular distribution of solidified melt tracks of approximate bimodal composition each less extreme than that of their respective constituent feed wires. The yield strength of the dual alloy composite material was approximately midway between that of the two alloys from which it was produced and exhibited a double inflection yield behaviour. Overall, because of the relatively coarse length scale there was not a significant property advantage in tensile loading above that of a chemically homogenous material, thus the main advantage of printing alternate alloys at this length scale is likely to reside more with increasing crack path tortuosity during fracture or fatigue loading. Importantly, the deposited material was found to have a refined β-grain structure suggesting that the composition gradients introduced by dual-alloy printing can disrupt the epitaxial columnar growth normally seen in WAAM deposits.

1. Introduction

Titanium alloys, like Ti–6Al–4V (Ti64), are in increasing demand for aerospace applications due to their high specific strength, corrosion resistance, damage tolerance, and compatibility with graphite fibre composite materials [1–3]. Owing to the high processing and machining costs associated with producing conventional wrought titanium products, the aerospace industry is currently evaluating the potential of additive manufacturing (AM) for producing large near-net-shape airframe components. This step up in scale requires higher build rates and lower costs than can be achieved with powder-based technologies. Of the different approaches available, wire fed Directed Energy Deposition (DED) processes, like Wire-Arc AM (WAAM) [1,4–6], have several advantages over other technologies including: a high material utilisation (99% [7–9]) and energy efficiency (~ 70% [8,10,11]), lower capital equipment costs, high kilogram-per-hour deposition rates [9], and large build envelops of several meters.

In addition to their greater near-net-shape capability, AM technologies can add value by taking advantage of the layer-by-layer deposition principle to 'print' components with tailored microstructures and compositions [12–19]. In WAAM, this can be more readily achieved than in a power bed process by using a dual wire feed system, or actively managing the thermal history experienced by each layer [20]. Benefits of this approach could include: functionally-graded properties (e.g. manufacture of components with a higher surface oxidation or wear resistance combined with a more creep resistant core [17,19,21,22]), or microstructures specifically designed to deflect cracks and increase fatigue life [21]. For example, Hernández-Nava et al. [21] *have* demonstrated, using a novel electron beam melting and hot isostatic pressing technique, that two microstructure types could be engineered for site-specific properties in a single component, whereby coarse colony α could be produced for areas where fracture-resistant properties were desirable, and fine Widmanstatten α for high yield-strength areas.

In a first step to investigate the feasibility and limitations of dual alloy printing Ti alloys with the WAAM process, here an extreme combination of hard and soft alloys has been studied using materials which were readily available, namely Ti64 (grade 5) and grade 2

* Corresponding author.
E-mail address: alec.davis@manchester.ac.uk (A.E. Davis).

https://doi.org/10.1016/j.msea.2019.138289
Received 30 July 2019; Received in revised form 12 August 2019; Accepted 13 August 2019
Available online 14 August 2019
0921-5093/ Crown Copyright © 2019 Published by Elsevier B.V. This is an open access article under the CC BY license (http://creativecommons.org/licenses/BY/4.0/).

commercially-pure Ti (CPTi) welding wire. However, it is widely recognised that production of Ti64 components by wire fed DED AM produces significant changes to the microstructure when compared with conventional wrought processing routes [6,20,23,24]. In particular, in WAAM, large columnar β grains can grow across many deposition layers, often spanning most of the full build height. These coarse grains evolve by epitaxial regrowth of the β grains that reform at the fusion boundary on reheating above the β transus temperature. In AM with Ti64, the solidification conditions favour columnar growth as a result of the steep thermal gradients in a moving melt pool and a lack of solute partitioning, which prevents nucleation ahead of the solidification front [6,24–27]. The β grains grow with their crystal < 001 > directions approximately parallel with the maximum melt-pool surface thermal gradient which, with stable build conditions, can produce a strong < 001 > fibre texture [26–30]. A texture memory is also translated through the Burgers orientation relationship (BOR) to the α phase on cooling which, although diluted by the 12 variants possible, can be detrimental to mechanical isotropy [31,32] and fatigue life [2,33].

The scanning heat source in AM processes also causes the deposited material to experience multiple heating cycles, with a decreasing peak temperature, as more layers of material are deposited. This cyclic heating can produce notable heat affected zone (HAZ) banding in Ti64 WAAM deposits, where coarsening of the α transformation microstructure occurs; as well as more subtle changes, such as an increase in the degree of α–β solute partitioning, and the formation of a finer α colony microstructure at the top of each HAZ band [1,6,20,23,24,28,34,35]. For example, Zhang et al. [1] have demonstrated that HAZ bands and texture can have a significant influence on the anisotropy of the fracture toughness and crack propagation in Ti64 WAAM.

The wrought α alloy grade 2 CPTi can have an elongation twice that of wrought α-β Ti64, although mechanical strength is sacrificed for this increased ductility [31,36,37]. This increased ductility can lead to a higher fracture toughness – a K_{1C} of 103 MPa $\sqrt{m}$ was reported by Sabirov et al. [38] which was higher than that for wrought Ti64 [38]. However, the fracture toughness depends critically on the oxygen content [1,36]. CPTi components have also been previously produced using WAAM [39], electron beam melting [40], and selective laser melting (SLM) [41,42], with tensile proof stresses as high as 555 MPa reported for the SLM process [42].

When using arc processes to join dissimilar alloys it is generally found that Marangoni driven convection and hydrodynamic forces from the arc pressure generally result in efficient mixing within the liquid phase. This leads to uniform liquid composition except close to the fusion boundary where a thin boundary layer is often observed [43]. Previous work on welding Ti64 to CPTi [44,45] has also demonstrated that, in addition to a narrow chemical mixing region at the fusion interface, alloying elements can diffuse a significant distance from the Ti64 into the CPTi, creating regions of lean Ti64 and alloyed CPTi (an effect also seen in Ti dissimilar metal combinations in AM [16,46]). When tensile tested, these dissimilar welds demonstrated good bonding, but the specimens had yield strengths similar to that of the weaker material (CPTi) and elongations similar to that of Ti64.

Previous work on printing dissimilar alloy combinations in AM has focused on the blown powder process (e.g. Refs. [46–48]) with little prior work reported with wired-based systems, and there is little detailed microstructural and property data on the effects of combining different Ti alloys. To date, rather than focusing on depositing alternating tracks of two or more materials, dissimilar-alloy printing has focused on depositing components with a single dissimilar-alloy weld (e.g. Refs. [46,48]), which will not benefit from the plastic constraint and elastic shielding effects seen in multi-phase or composite materials [49,50], effects that could potentially be exploited from an alternating track build. However, several studies have been conducted, using blown powder techniques, to deposit graded Ti alloy microstructures from α [18,51] or α+β [13] compositions to 100% β compositions, to investigate the α and β microstructural distributional changes, and the hardness behaviour across such graded structures. Recent work using field assisted sintering of Ti64 to CPTi has also shown that the composition gradient across the interface can result in strong microstructure and hardness gradients in certain titanium dissimilar alloy systems [52].

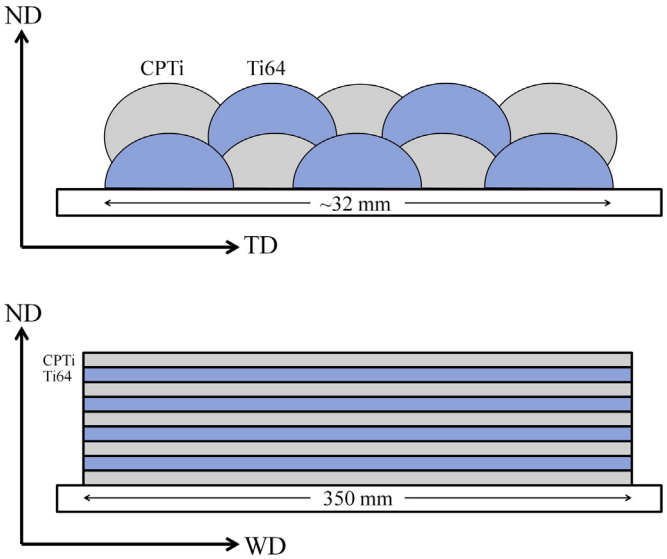

Fig. 1. Schematic diagram of the dual alternating alloy 'AAC' WAAM deposition strategy employed; where WD = the heat source travel direction parallel to the wall, TD = the wall transverse direction, and ND = the build height direction perpendicular to each layer.

The aim of this investigation was therefore to more rigorously investigate the metallurgical viability of producing large scale titanium structural parts with alternating controlled compositions by the WAAM process, following re-melting and some inevitable dilution; and to determine any improved static properties and thus shed light on possible application areas using a hard/soft model component. To this end, a dual titanium alloy WAAM – or 'alloy-alloy composite' (AAC) – linear wall was built using alternating beads of Ti64 and CPTi with parallel deposition tracks, following the scheme shown in Fig. 1. The work has focused on determining the extent and pattern of material mixing, and the potential effects of this on the microstructure within the boundary layer composition gradients; as well as whether any microstructural and mechanical-property advantages could be achieved over either individual alloy, based on tensile and fracture toughness tests. For example, in a dual alloy system the possibility exists that the softer CPTi deposits may experience an increase in yield stress due to the plastic constraint acting upon it from the harder Ti64 tracks, an effect demonstrated previously in multi-phase steels [50]. The alternating deposition pattern of the CPTi and Ti64 also has potential to control the failure crack path in the component, so the feasibility of crack-path control, and the possibility of improved fracture toughness, has been investigated.

2. Materials and methods

The 350 × 100 × 32 mm AAC WAAM wall studied was produced using two separate 1.2 mm diameter wire feedstocks comprised of grade 2 CPTi and Ti64, the nominal compositions of which are given in Table 1. Two wire feeders were used to build a simple linear 10 track wide wall, 60 layers high, using parallel tracks with a constant raster direction in an alternating pattern with a constant wire feed rate, as shown in Fig. 1. This resulted in a 50:50 volume ratio of each alloy wire deposited within the wall. The sample was produced on a Ti64 substrate using a plasma arc process head and a local argon shielding

Table 1
Composition of the CPTi and Ti64 wire feedstock (wt.%).

Material	Ti	Al	V	Fe	O	N	C
Ti64	BAL	6.09	3.92	0.19	0.14	0.01	0.01
CPTi	BAL	0	0	0.05	0.11	0.01	0.03

Table 2
WAAM process parameters.

Working distance	8 mm	Plasma gas flow	0.8 l min^{-1}
Wire feed speed	2 m min^{-1}	Shielding gas flow	20 l min^{-1}
Travel speed	4–4.8 mm s^{-1}	Interlayer height	1.5–1.7 mm
Current	180 A		

device, with the parameters provided in Table 2. The wall reference frame is defined as: WD = the heat source travel direction parallel to the *wall*, TD = the wall *transverse* direction, and ND = the build height direction *normal* to each layer. After deposition, the wall was stress relieved by heat treatment for 2 h at 540 °C, before removal from the substrate for testing and analysis.

Flat, 1.6 mm thick, tensile specimens were extracted from the WAAM wall as shown in Fig. 2a with orientations ND-TD and WD-TD; where the first direction is parallel to the gauge length, and the second normal to the specimen plane. The tensile specimens had a gauge length and width of 30 and 6 respectively. The specimens were strained at room temperature at a nominal rate of 0.05 min^{-1} until failure. The tensile tests were repeated 9 times in each sample orientation, then averaged and given 95% confidence intervals.

Fracture-toughness test specimens were extracted from the WAAM wall, as shown in Fig. 2a, with dimensions provided in Fig. 2b. To satisfy the conditions for plain-strain fracture toughness (K_{1C}) determined by ASTM E399 [53], fracture-toughness samples of this design must have a thickness of over 40 mm. It was not possible to obtain AM samples of this thickness; therefore we have used K_Q values, which overestimate K_{1C} values, but allowed valid comparisons for a consistent thickness and sample geometry. The samples were machined with orientations WD-ND and ND-WD, where the first direction corresponds to the crack growth direction and the second is normal to the specimen crack plane i.e. samples were tested with cracks propagating parallel (in the plane of) and perpendicular to the deposited layers. All tests were performed in accordance with ASTM E399 at 22 °C and 50% humidity, using an average loading rate of 38 kN min^{-1}.

Fracture surface topographies were analysed using a Keyence VHX-5000 digital microscope, which allowed a fully-focused stitched image map to be reconstructed with 3-dimensional information for whole fracture surfaces. Samples for optical and scanning electron microscope (SEM) observation were metallographically prepared using standard procedures and an OPS suspension mixed with 5% hydrogen peroxide as a finishing polish. The samples were etched in Kroll's reagent for optical microscopy, which was performed using a Zeiss Axio Imager 2 with automated image stitching capability. Hardness maps were generated using a Struers Durascan 80 auto-hardness tester, from an array of indents with a pitch of 0.35 mm, on polished samples with an applied load of 0.3 kg and dwell time of 10 s.

SEM imaging, electron backscatter diffraction (EBSD) orientation mapping, and energy dispersive X-ray spectroscopy (EDS) elemental mapping were conducted using a Tescan Mira3, FEI Magellan, or FEI Sirion field emission gun SEMs, equipped with Oxford instruments EBSD and EDS systems. α inter-lamellar spacings (α_{ILS}) were measured from backscatter electron SEM micrographs (1 image per measurement) using the standard linear intercept method corrected to compensate for diagonally-orientated lamellar [20,35]. Error was given as 95% confidence intervals.

The EBSD and EDS maps were acquired with an accelerating voltage of 20 kV and a step size of 9 and 10 µm respectively to generate large-area maps to evaluate mixing, β grain structures, and texture. The qualitative EDS signal intensity maps were smoothed and assigned jet colouring in ImageJ [54]. The EBSD maps were processed using Oxford Instruments HKL CHANNEL 5 software and are shown in inverse pole figure colouring. Texture data is presented in standard pole figures with intensities given in multiples of random density (MRD). Reconstructed β-phase orientation maps were produced from the α-phase EBSD data using software developed by Davies and Wynne [55,56] (based on [57,58]) that calculates the β-phase parent orientations from the BOR, within an allowed 2° misorientation error to match a particular α variant, as well as a 3° divergence from the ideal BOR to match an α variant to a parent β orientation.

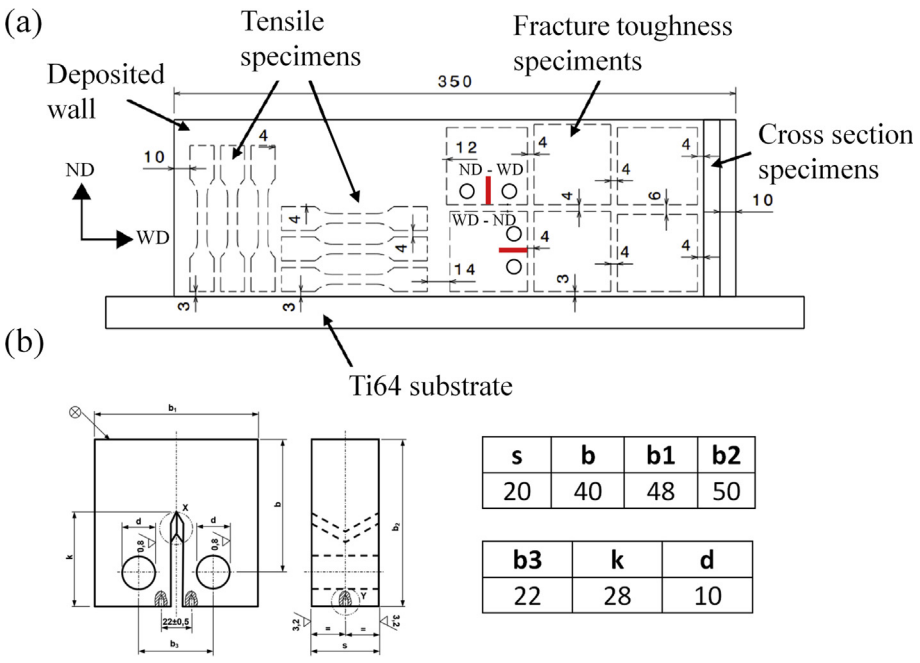

s	b	b1	b2
20	40	48	50

b3	k	d
22	28	10

Fig. 2. (a) Specimen extraction map and (b) plane-strain fracture-toughness sample geometry. All measurements in mm.

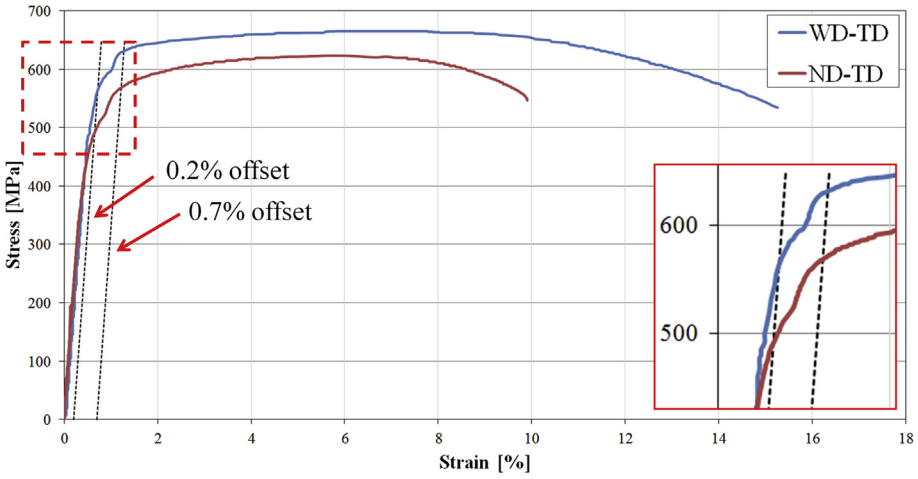

Fig. 3. Example tensile stress-strain curves recorded for the AAC WAAM specimens cut with the gauge length in the heat-source travel direction (WD, with width parallel to TD) and gauge length aligned in the vertical build-height direction (ND, with width parallel to WD, see Fig. 2a). The unusual double inflection yield behaviour is highlighted in the magnified insert. Note the positions of the 0.2% and 0.7% elastic off-set lines.

Electron probe microanalysis (EPMA) maps and line scans were performed on a JEOL JXA-8530 F FEG-EPMA equipped with 4 wave dispersive spectrometers (WDS) and EDS. 1 × 1 mm area maps were scanned at 15 kV and 100 nA with a 40 m s dwell time and a 1 μm step size, with counts for aluminium ($K_{\alpha 1}$) collected on a TAP diffraction crystal, and iron ($K_{\alpha 1}$) and vanadium ($K_{\beta 1}$) on a LiFL diffraction crystal. Line scans were extracted from the maps taking averages from 5 × 5 kernels for each point, which were then given 95% confidence intervals.

3. Results and discussion

3.1. Mechanical properties

Example tensile stress-strain curves for the alloy-alloy composite WAAM specimens, tested with their tensile axis parallel to the heat-source travel or build-height directions, are provided in Fig. 3 and the averaged tensile test data measured from 9 test samples for each condition is summarised in Table 3. Overall, the results show that, similar to other continuously reinforced composite materials [59], the AAC-WAAM deposits gave a better all-round mechanical performance when tested parallel to the direction of alignment of the alternating alloy tracks (in WD), compared to when tested in the direction normal to the deposited layers (ND). From Fig. 3, it can be seen that the 0.2% proof stresses were approximately 20% higher in the travel direction compared to in the build direction. This was, however, ~ 270–300 MPa lower than for a comparable Ti64 monolithic, single bead wide WAAM wall [31,34], but 60% higher than for a typical wrought grade 2 CPTi product (Table 3). In addition, a distinctive double inflection yield response was observed in the stress-strain curves in both loading directions (highlighted in Fig. 3) which affected the 0.2% proof stress values.

The position of the 0.2% offset elastic loading line shown in Fig. 3 indicates that this measure of yield stress effectively recorded the 'lower' yield point. In fact, the 0.2% offset proof stress values are similar to that expected from CPTi built by an SLM AM process (Table 3). Although there is no data currently available for WAAM material produced in grade 2 CPTi, previously published results for AM deposits produced by SLM and EBM have yield stresses in the range 360–555 MPa (e.g. Refs. [40,42]), while wrought CPTi products typically have lower yield stresses in the range 275–410 MPa [3]. This demonstrates that in both loading directions, yielding occurred first in the weakest phase present (i.e. the deposited CPTi) which then rapidly strain hardened, and due to constraint [50], transferred load to the stronger more highly alloyed regions, as shown in the magnified yield response insert in Fig. 3. As will be shown below, in the WAAM material all of the weaker 'phase' was enriched in solute from the Ti64 alloy and this is mainly responsible for the increase in yield stress over that of a CPTi wrought material [2,60], whereas in the SLM power bed process the much higher cooling rate results in a higher CPTi as-built strength due to the finer microstructure.

It can further be seen in Fig. 3 that the 'higher' yield point inflections (580 MPa in ND and 640 MPa in WD), which have also been characterised here using a 0.7% offset, are still lower than expected for the Ti64 parent material. Additionally, the AAC WAAM samples had a 0.2% proof stress anisotropy of 0.84 with respect to the travel direction, which is slightly lower than that typically seen for Ti64 WAAM [31,34]. The UTS values measured for the AAC samples were also approximately 25% lower than that for a typical monolithic WAAM Ti64. These 'upper' yield stress values are, however, not out of line with what might be expected from a simple 'rule of mixtures calculation' [61], which would give a tensile yield strength of 623 MPa for a 50:50 CPTi (produced under EBM conditions) and Ti64 mixture parallel to the wall, based on the yield stress values presented for the monolithic alloys in Table 3.

The elongation to failure of the AAC WAAM samples was also asymmetric, being 50% greater in the travel direction than in the build direction, which is the opposite trend to that seen in Ti64 WAAM materials, where the coarse β-grain structure generally leads to a poorer WD ductility [31,34]. No substantial improvement to elongation was

Table 3
Tensile and fracture toughness results for the AAC WAAM measured in this work compared to that taken from Ti64 WAAM published in the literature [31,34]. The CPTi data is for selective laser melting (SLM) and electron beam melting (EBM) published data [40,42]. Wrought grade 2 CPTi data was taken from Ref. [3].

Material	Direction (gauge - crack)	$\sigma_{0.2}$ [MPa]	$\sigma_{0.7}$ [MPa]	UTS [MPa]	ε [%]	K_Q[MPa$\sqrt{m}$]
AAC (CPTi–Ti64)	Build (ND)	497 ± 11	568 ± 17	615 ± 18	12.8 ± 1.5	82.8
	Travel (WD)	594 ± 19	648 ± 21	684 ± 18	19.7 ± 0.7	77.8
Ti64 [33][a] [36],[b]	Build (ND)	810 ± 20[a]		890 ± 10[a]	20 ± 2[a]	81.9[b]
	Travel (WD)	870 ± 30[a]		920 ± 20[a]	12 ± 5[A]	73.9[b]
CPTi SLM [42]	Build (ND)	555 ± 3		757 ± 13	20 ± 2	
EBM [40]	⊥ to build	360–390		460–490	~30	
CPTi (wrought) [3]		275–410		345–550	15–35	66

therefore gained by using the AAC build strategy over a conventional Ti64 WAAM monolithic wall. However, it is worth noting that previously published elongation data for Ti64 WAAM [31,34] as well as being lower in the horizontal direction has much greater scatter, demonstrating an undesirable unpredictability, which was not the case for the AAC-WAAM build which failed in a much more repeatable fashion with a scatter of < 1%.

A summary of the fracture toughness results for the AAC WAAM is also provided in Table 3. Due to the restricted sample thickness, it was only possible to obtain K_Q values as the width requirement for K_{1c} were not met (in accordance with ASTM E399 [53]). Nevertheless, the results show that the fracture toughness was 6.4% greater when the crack propagated in the build (ND) direction across the TD-ND plane, relative to when it propagated in the travel (WD) direction in the TD-ND plane. When compared to published data for Ti64 monolithic WAAM materials [1], the AAC samples were found to have a similar fracture toughness to monolithic Ti64 when tested in the build direction, but exhibited a small improvement in the travel direction.

Overall, it can be anticipated that the mechanical behaviour of the AAC samples will have been highly influenced by the volume fractions of the different compositional zones, produced by the mixed melting and subsequent solidification-microstructural response of the alternating alloy tracks, and their geometric arrangement with respect to the loading/crack propagation direction, which will strongly affect the strain distribution and failure path. These important aspects of an AAC's behaviour will be explored further below.

3.2. Macrostructure

Optical macrograph cross sections of the as-deposited AAC-WAAM component are presented in Fig. 4 for the WD-ND and TD-ND planes. Due to their locally varying compositions, the samples were difficult to prepare and are not simple to interpret in terms of the chemical distribution, but did reveal the parent β-grain structure and the presence of microstructural banding. The TD-ND transverse cross section is therefore accompanied by a large area SEM-EDS Al map in Fig. 4c, which shows a regular 'fish scale' pattern for the Al distribution caused by the overlapping CPTi and Ti64 alternate alloy tracks. Image analysis from Fig. 4c revealed that the volume fraction of the residual CPTi melt tracks was ~ 33%, which is smaller than that of the residual Ti64 alloy tracks, despite identical build parameters and wire feed rates being used for each alloy. Even though a regular repeating pattern of alloy tracks can be observed in the EDS map, a significant Al count rate was found across the entire volume of the CPTi beads and a lower than expected Al composition in the Ti64 rich deposits. The extensive intermixing that has thus clearly occurred between the alternate deposition tracks will be explored further below using results from the quantitative, higher resolution EPMA technique.

In comparison to a conventional monolithic Ti64 WAAM build, it is also interesting that in the AAC-WAAM sample, the β-grain structure appears significantly finer in the optical images than would normally be expected [6,24]. The level of grain refinement found in the duplex alloy deposit can be more reliably determined from the reconstructed $\beta-$phase EBSD map shown in Fig. 5b, where it can be seen by comparison with Fig. 4c that grain growth during solidification in ND seems to have been disrupted by the solute rich and lean layers within the material. Although still columnar in nature, the grains in the AAC sample have a length in ND of < 3 mm – which is equivalent to ~ 2 layer heights – and are less than ~ 1 mm in width (TD). In contrast, in a single alloy Ti64 WAAM build, the columnar grains typically extend over multiple layers and can be centimetres in length [6,24–27]. In addition, a small number of isolated near-equiaxed 300–500 μm diameter grains can be seen distributed throughout the cross section, which are also not generally found within a monolithic Ti64 walls. From closer examination of Fig. 5c, it is apparent that there is again a correlation between these refined grains and the local composition, with most of the near-equiaxed grains appearing to be located at the transition between the solute-rich and solute-lean layers in the deposit.

Although the sampling statistics are generally too poor to determine a reliable texture strength by EBSD measurements (due to the extremely large grains size in WAAM samples), the overall reconstructed β texture depicted in the pole figures measured here (Fig. 5d) is weaker than that typically reported for conventional monolithic Ti64 WAAM deposits (~9× peak intensity compared to > 20× MRD [26,62]). The pole

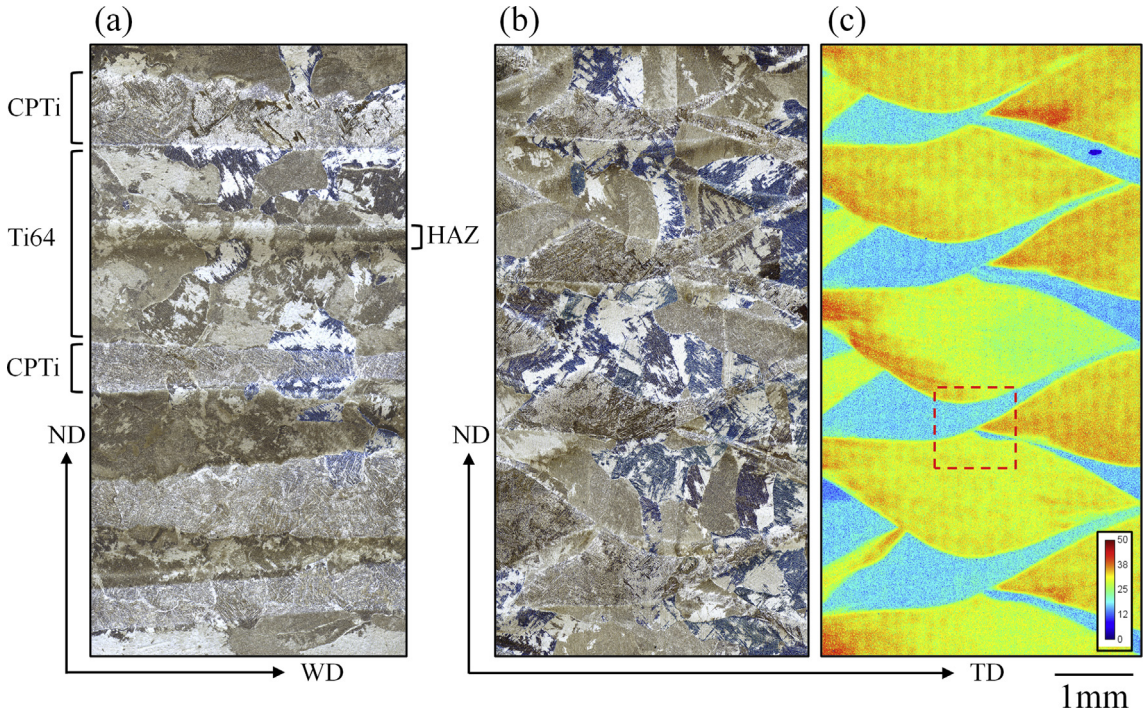

Fig. 4. Optical macrographs of the AAC WAAM component viewed in (a) the WD-ND and (b) TD-ND planes. In (c) a large area SEM-EDS Al counts per second compositional map is presented for comparison with (b). (The highlighted region in (c) is the area analysed in more detail by EPMA – see Fig. 7).

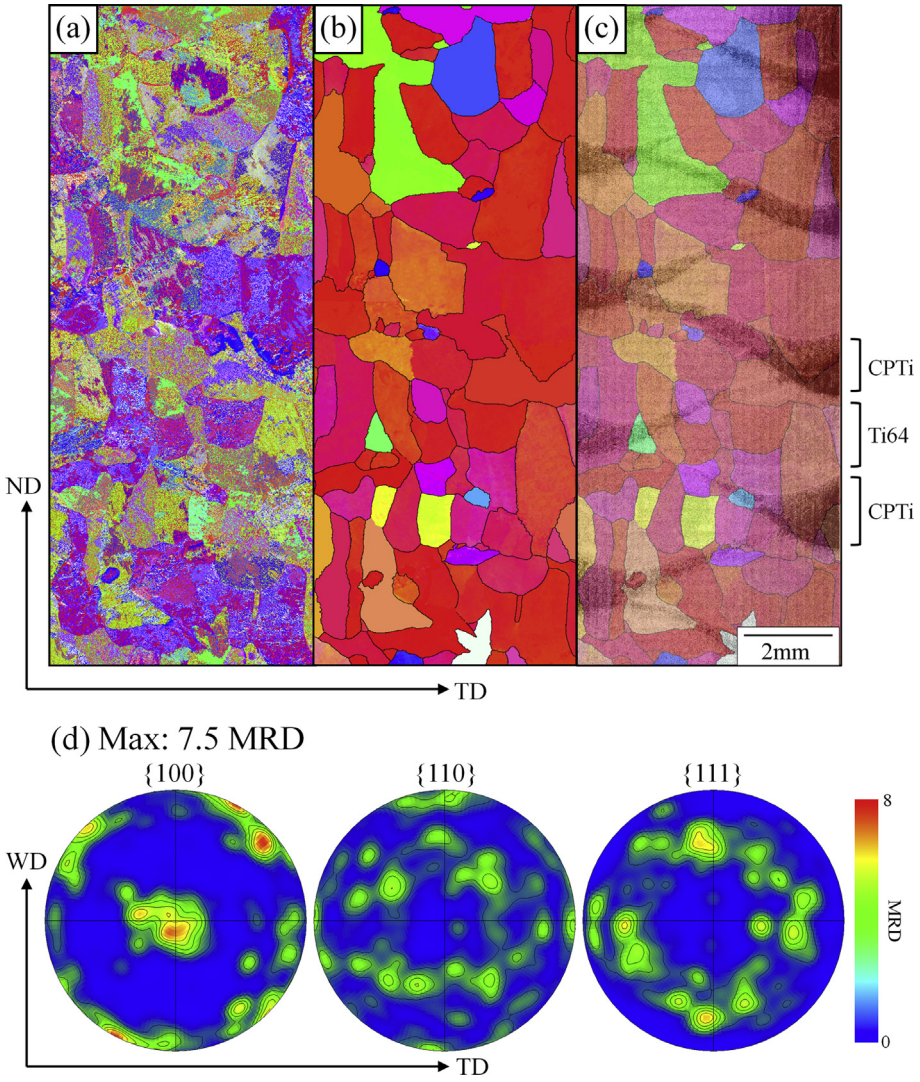

Fig. 5. Large-area EBSD maps of the AAC WAAM build, from the TD-ND plane, in IPF colouring (with respect to ND): (a) the α-phase map, (b) the reconstructed β-phase map, and (c) the reconstructed β-phase map overlaid on the enhanced pattern-quality (band contrast) map to reveal the position of alternate alloy layers. In (d), β-phase pole figures are provided from (b) in multiples of random density (MRD).

figures for the AAC material do, however, still show a strong common preferred < 001 > direction close to ND. In addition, while the statistics in Fig. 5d are insufficient to determine if there is a true random distribution around the < 001 > //ND fibre, the data suggests some preferred alignment in the build plane of the < 001 > poles at ~ 45° to WD.

The etching contrast in the optical images shown in Fig. 4 further revealed narrow white (less etched) bands at the fusion boundary/interface between each CPTi–Ti64 deposit, and wider HAZ bands within the Ti64 layers [6,20]. These two types of bands are more readily apparent in the WD-ND image (e.g. Fig. 4a) due to their linear nature, whereas in the TD-ND plane the heat source, as well as the alternating alloy distribution, produces a more complex overlapping fish-scale pattern due to the curved melt pool surface and curved thermal field shape generated when the tracks are overlapped laterally in the WD-TD plane.

In Fig. 6a, a contoured microhardness map has been overlaid on an optical macrograph of the AAC WAAM sample. A hardness profile across a typical area is also provided in Fig. 6b. The map and hardness profile show that the majority of the local hardness distribution is split into two relatively narrow ranges of 180–210 and 250–280 H_V, which reflects the positions of the alternating Ti64 and CPTi wire-fed deposition tracks which had average hardness levels of ~200 H_V and ~260 H_V respectively. These bimodal hardness levels are substantially less than that of conventional Ti64 WAAM (~ 340–370 H_V [23,24,52,63]), which suggests that extensive mixing has taken place between the alloys to produce a material consisting largely of two regions of relatively consistent composition, based on enriched CPTi and diluted Ti64. Separating the hardness map into two bins of above and below 220 H_V shows that the harder regions dominate approximately two thirds of the microstructure. Very small areas with significantly higher and lower hardness levels can also be seen in the map – these maximum hardness regions had peak values of ~ 320 H_V, which is still considerably lower than that of Ti64; whereas the softer regions had a minima of ~ 150 H_V, which is closer to that expected for CPTi with a low oxygen content [52]. The maximum hardness levels were only found within the occasional overlap areas between two Ti64 deposits, and contributed less than 4% of the volume fraction of the entire build, whereas the centre of the vast majority of the Ti64 wire tracks had harness levels lower than 300 H_V, further demonstrating the strong effect of dilution of the majority of the Ti64 alloy that has occurred during deposition by mixing with CPTi.

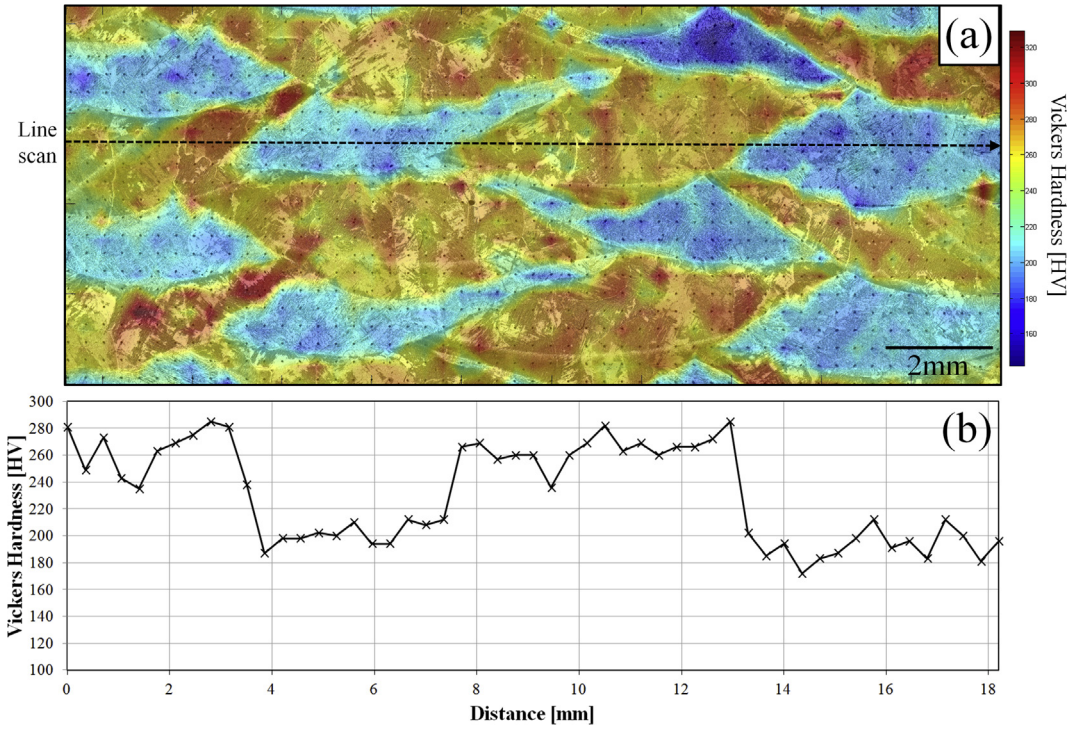

Fig. 6. (a) Microhardness map (H_V) of the AAC WAAM sample (TD-ND section) overlaid on an optical macrograph. In (b) an example profile across TD is given for the single line of indents shown in (a).

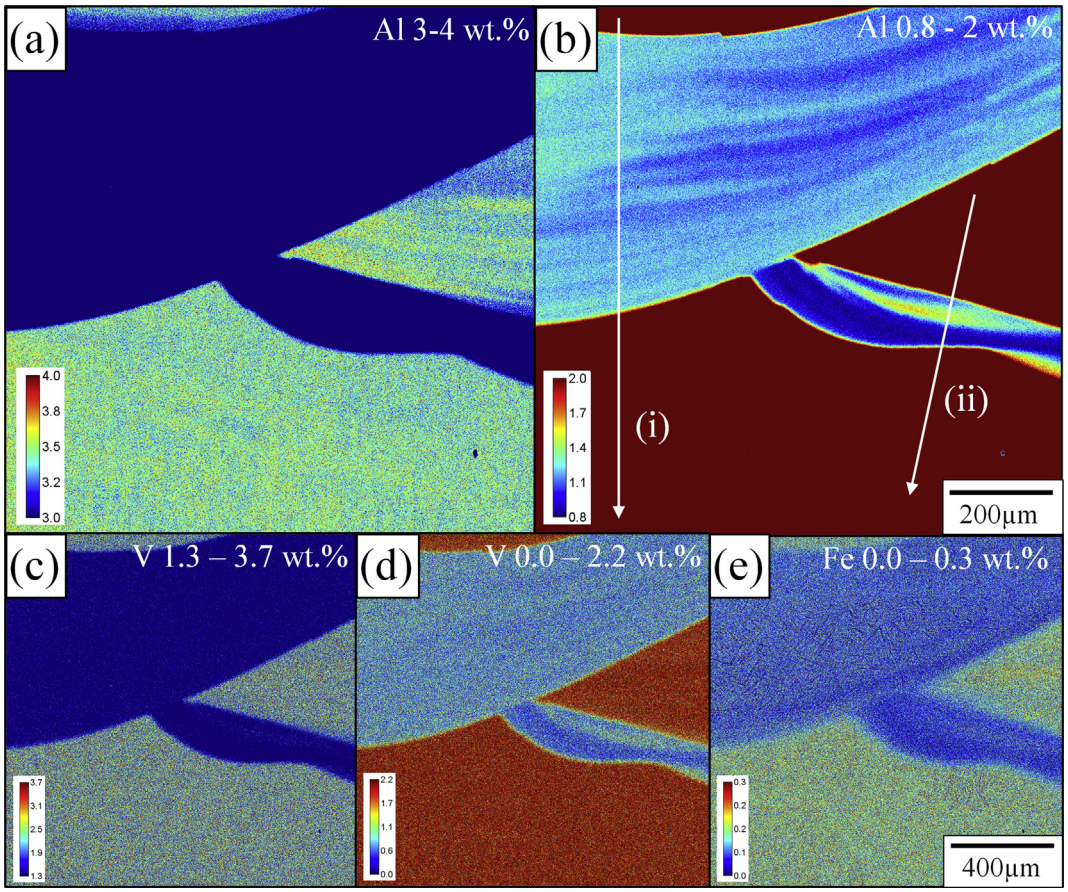

Fig. 7. Quantified EPMA chemical maps from the AAC WAAM component taken from a representative repeat region in the ND-WD sample section, shown qualitatively in Fig. 4c: (a–b) Al maps at different scales, (c–d) V maps at different scales, (e) Fe. All scale bars are in wt. %.

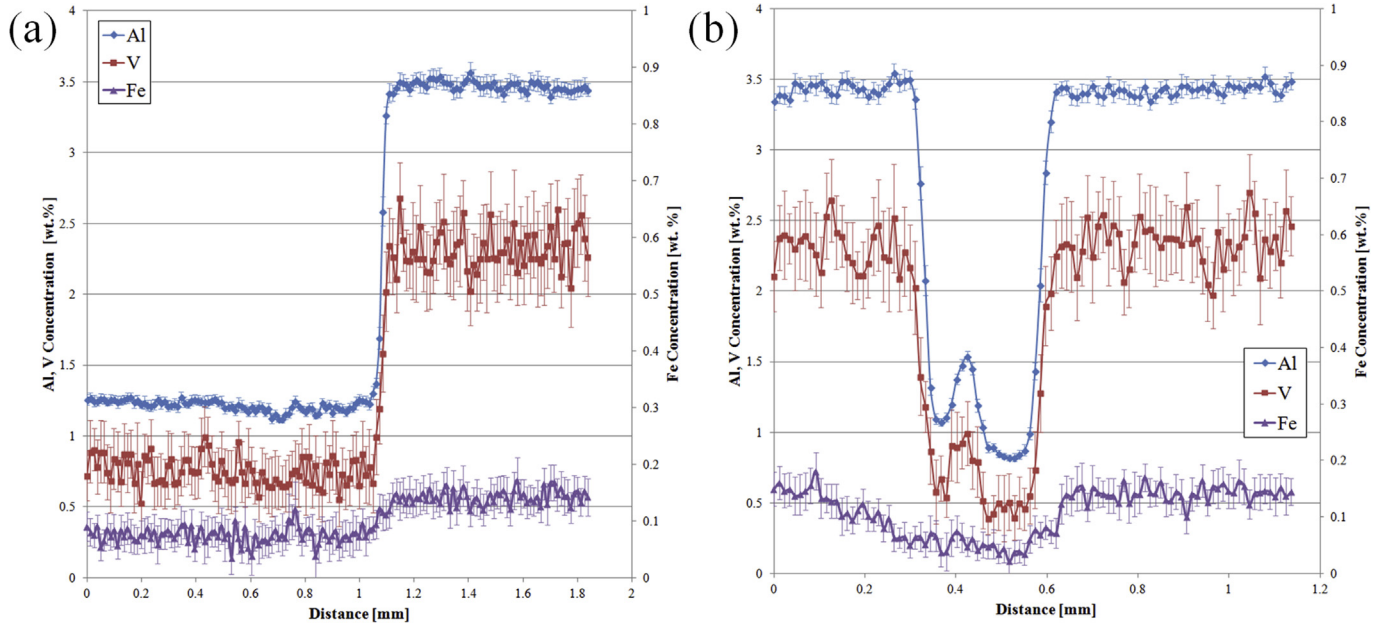

Fig. 8. Quantified EPMA line scans along positions annotated on the Al map in Fig. 7: (a) line (i), (b) line (ii).

3.3. Chemical analysis

Quantified, higher resolution EPMA chemical maps are provided in Fig. 7 over a representative deposition pattern repeat unit cell, identified in the ND-WD sample section shown in Fig. 4c. The EPMA maps show the distributions of Al, V, and Fe, using different concentration ranges to better highlight the solute distribution in the CPTi and Ti64-rich deposits. It is immediately apparent that when depositing the AAC sample, large scale mixing has occurred from track overlap and substrate re-melting, which in the region analysed, has alternately produced a diluted form of Ti64 and alloyed, enriched CPTi. This interpretation also agrees with the majority of the area of the large-area hardness and EDS maps, which suggested there were few remaining regions of unalloyed CPTi or undiluted Ti64 after deposition, and that the majority of solute rich (Ti64 wire deposit) and solute lean (CPTi wire deposit) regions both had a modified, but relatively uniform composition. A sharp compositional gradient can also be seen between the two distinct compositional regions in Fig. 8, resulting in the majority of the material being comprised of two chemically distinct nominal compositions of approximately Ti-3.5Al-2.3 V and Ti-1.3Al-0.7 V. This has occurred because there has been a relatively consistent dilution of each alternate alloy wire deposited, when fed into the melt pool formed with the re-melted substrate, as well as a high level of mixing in the liquid due to melt pool hydrodynamics [64]. For example, in the quantified line scans in Fig. 8, the Al distribution can be seen to segregate into bands varying from ~ 3–3.6 wt% and ~ 0.8–1.2 wt% in each material region respectively. The line scans also show that the boundary layer between the two chemically distinct regions undergoes an abrupt change in composition, which is only ~ 70 μm wide. The boundary layer is also similar in width to that of the thin etched-white boundaries seen in the optical images in Fig. 4.

Although the composition variation can, therefore, in most areas be approximated as being close to a binary step function (e.g. Fig. 8a), when the EPMA map composition scale is stretched to highlight the concentration variation of each individual element (Fig. 7) it becomes more apparent that complete mixing has not occurred in the liquid phase. For example, in Fig. 7b there is evidence of shear layers of locally different liquid composition produced by the melt pool fluid flow. It is thus apparent that due to the short interaction time experienced in a welding-based process, inter-diffusion between the mixed liquid shear layers has remained partially incomplete. However, this variation was relatively modest being less than ± 0.3 wt% for Al and V. Finally, the Fe concentration was also found to vary between the solute rich and solute lean regions, owing to the slightly higher trace level permitted in Ti64 compared to in grade 2 CPTi welding wire. Fe also showed a more diffuse transition across the boundary layer region between the alloy rich and lean layers than Al or V. This could be a result of the lower partition coefficient for Fe compared to Al and V (i.e. $k_{Fe} = 0.38$, k_{Al}, $k_V \approx 1$ [65,66]), which has been noted to cause stronger solute partitioning at the fusion boundary in Ti64 deposits [20]; but could also be influenced by the unusually high solid state diffusivity of Fe in BCC titanium relative to Al and V [67], which may have caused greater inter-diffusion of the Fe during subsequent thermal cycling.

3.4. Boundary layer transformation microstructures

In any bimodal material it is important to understand the microstructural transition between each compositionally distinct region. SEM images taken systematically across the EPMA-scan area in Fig. 7, and another similar representative unit of systematic composition variation between two alternating deposition tracks are provided in Fig. 9b and c, where the solute rich and lean layers have been distinguished using EPMA and SEM-EDS respectively. The selected areas are highlighted with respect to their position in the build in Fig. 9a. In Fig. 9b and c, the solute-lean CPTi deposition track regions can be seen to have an overall coarser α lath structure, whereas the Ti64 rich region has a finer basketweave Widmanstätten microstructure, as is more common for Ti64 monolithic materials deposited by WAAM [6,20,39,40,42,52]. There also appears to be a transition region between the two regions towards the CPTi–Ti64 fusion boundary (marked by the dotted red line) which is ~ 50 μm wide, consistent with the narrow composition boundary layer width seen in Fig. 8.

In Fig. 9d the α inter-lamellar linear intercept spacings (α_{ILS}) measured from SEM images for each position is plotted against distance across the CPTi–Ti64 track interface from the area shown in Fig. 9b, alongside the Al concentration and measured β-phase fraction (β_f) predicted using the local EPMA composition data in the proprietary CALPHAD software JMatPro [68]. A similar plot is provided in Fig. 9e for the area shown in Fig. 9c for the α_{ILS} and Al concentration (SEM-EDS). Both plots clearly show an overall increase in the inter-lamellar α

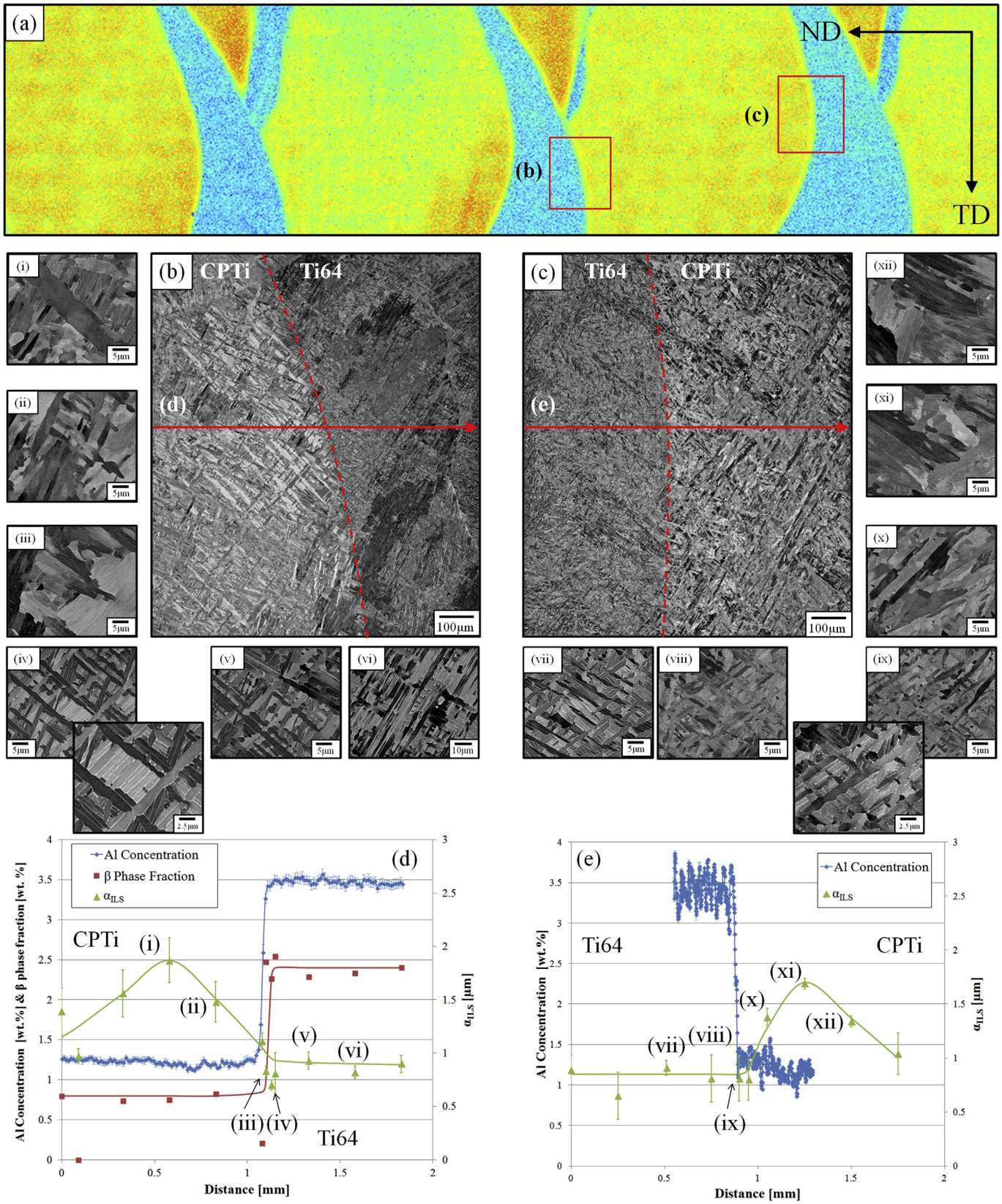

Fig. 9. (a) Al SEM-EDS map from Fig. 4c showing the areas where backscatter electron images (b) and (c) were taken from, where each shows the intersections of Ti64 and CPTi wire beads in the AAC WAAM component. (d) and (e) show the change in α inter-lamellar spacing as a function of distance across the CPTi–Ti64 interfaces in (b) and (c) respectively, and (d) additionally shows the Al concentration change measured from EPMA (Fig. 8a) and modelled β-phase fraction change across the boundary, and (e) includes the Al SEM-EDS measurement (counts per second) across the boundary.

between the enriched CPTi and diluted Ti64 deposits, as well as a reduction in the β-phase volume fraction in the more dilute CPTi track. However, there is also locally an increase in the α_{ILS} of ~ 1.25 μm in both alloyed CPTi tracks (seen in Fig. 9i and ix) which exhibit a peak in their lamellar spacing approximately 500 μm away from the CPTi–Ti64 track interface in each case. This increase occurred away from the boundary layer where the composition was uniform and cannot be ascribed to the effect of alloying. This local increase in α_{ILS} is, therefore, most probably caused by the same cyclical variance reported across HAZ bands in Ti64 monolithic WAAM builds [20], where rapid coarsening of the α lamellar spacing arises due to re-growth of the β phase, when the α microstructure is reheated towards the β transus during deposition of the subsequent track. This mechanism has been ascribed to transformation assisted coarsening, where the residual inter-lamellar β in the Ti64 WAAM α microstructure starts to regrow at above ~ 850 °C [69] consuming the smaller α lamellar, so that only the surviving α lamellar grow back on cooling. In the present case, the lower concentration of the slowest diffusing element V (~ 1.6 wt% V less) in the solute lean layer may allow the inter-lamellar β boundaries to migrate faster during the α-β transformation than in the Ti64-rich deposit. Thus, the larger starting α_{ILS} and the higher β-boundary velocity probably both contribute to the exacerbated increase in α_{ILS} within the CPTi-deposit HAZ band.

It should be noted that equivalent peaks are not seen in the Ti64-rich side of the boundary layer in the α_{ILS} results in Fig. 9d and e as the HAZ bands on the Ti64-rich side were outside of the studied region (Fig. 4a shows the HAZ bands are more than 1 mm from the CPTi–Ti64 deposit interface).

3.5. Fracture behaviour

The fracture behaviour of the longitudinal (WD) and build direction (ND) AAC-WAAM tensile test samples are compared in Fig. 10, using optical microscopy sections from their failure position parallel to the tensile axis. When tested perpendicular to the layers in ND, it can be seen that strain within the gauge length and neck formation has localised in the weaker alloy-lean CPTi layers (arrowed), which has ultimately developed into a neck that failed by ductile tearing with a high local plastic strain (reduction in area of ~ 35%). This greater strain localisation has reduced the overall elongation to failure in the ND tensile samples to 50% of that of the WD sample. When tested in the direction of the deposition tacks (WD) it was more difficult to distinguish the effect of the systematic composition variation of the individual tracks and it is apparent the sample has undergone more uniform plastic deformation, with more diffuse necking. In the necked region, both the solute rich and lean phases have been heavily deformed as they are effectively loaded in parallel and must both deform in unison to maintain plastic compatibility.

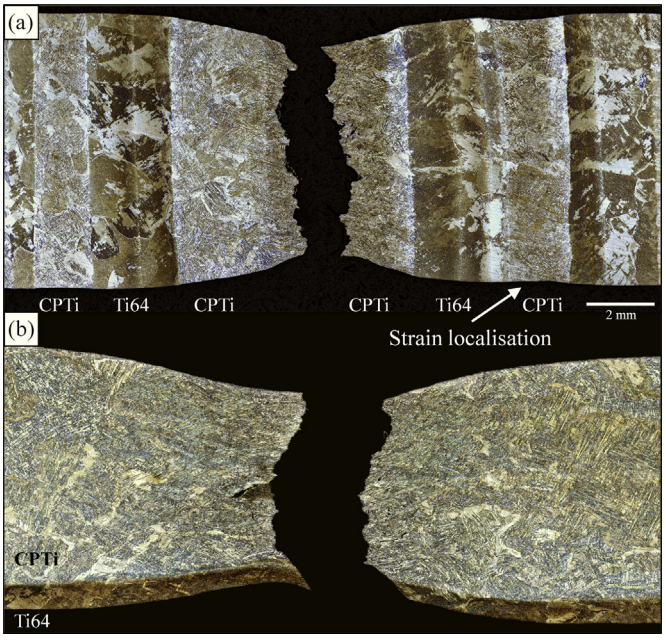

Fig. 10. Optical macrographs from tensile test specimens sectioned through their necked failure region at the mid plane for samples tested parallel to (a) the build direction and (b) the travel direction. The arrow in (a) indicates strain localisation within the softer diluter CPTi track.

3D surface scans, and fracture-surface SEM and cross-section optical macrographs are also provided for the fracture-toughness specimens in Fig. 11. In the WD-ND samples, where the crack propagated in the plane of the deposited layers in the heat-source travel direction (WD), it can be seen that the fracture path clearly followed the weaker solute-lean residual CPTi material, which resulted in the jagged path seen in the transverse direction in the optical macrograph, and was therefore clearly strongly influenced by the geometric arrangement of the solute-rich and solute-lean deposition tracks (Fig. 11c). In this case, because in this test orientation the deposition strategy created a relatively planar interconnected alloy-lean percolation path, the crack was able to follow the softer residual CPTi track deposits with only limited deviation. At low magnification, the fracture surface (Fig. 11b) did, however, exhibit a systematic macroscale roughness that was clearly controlled by the inter-connected geometry of the softer alloy-lean tracks. At a finer scale, the SEM micrographs (Fig. 11a) show that the softer low alloy content CPTi rich layers failed by a highly ductile fracture with a small number of porosity or lack of fusion defects apparent on the fracture surface.

In comparison to the WD-ND fracture toughness samples, with the ND-WD samples the cracks propagated in the ND direction (i.e. normal to the solute rich and solute lean layers). In the corresponding crack-plane cross sections shown in Fig. 11f, it can be seen that in this case there is no obvious preferred failure path and the crack crosses the low solute CPTi and high solute Ti64 region boundary layers without any evidence of systematic deflection. Indeed, the fracture surface roughness seems to be more closely related to the refined grain structure and has, therefore, been more influenced by large crystallographic misorientations between regions of different local α texture than the composition bands. At the macroscale (Fig. 11e), the fracture surface consequently shows less roughness than in the WD-ND sample and is almost flat across the bulk of the sample, with a shear fracture occurring at the samples edges. However, higher magnification SEM images in Fig. 11d reveal a more mixed-mode fracture surface, with regions exhibiting stronger crystallographic faceting and lower micro-roughness, as well as regions where there is more plasticity and micro-void coalescence [24,45,70]. This behaviour is indicative of the crack alternately crossing harder Ti64-rich filaments and the softer solute-lean bands within the duplex microstructure.

Finally, in both fracture toughness and tensile test orientations there was no evidence of the fracture behaviour being influenced by a weakened or brittle interface between the two materials. This is not unpredicted, as few defects were observed in the samples and no undesirable metallurgical reactions are expected from diluting Ti64 with CPTi, but this may not always be the case with other alloy combinations that create harder or brittle interface layers [45,46,52].

4. Discussion of the potential for producing AACs by the WAAM process

In a first step to evaluate the potential for taking advantage of additive manufacturing to tailor Ti materials when producing large-scale parts, an alloy-alloy composite WAAM component was built using a simple unidirectional alternating CPTi and Ti64 wire feed deposition strategy. This test case was produced to evaluate the likely compositional complexity of such duplex materials and the effect this might

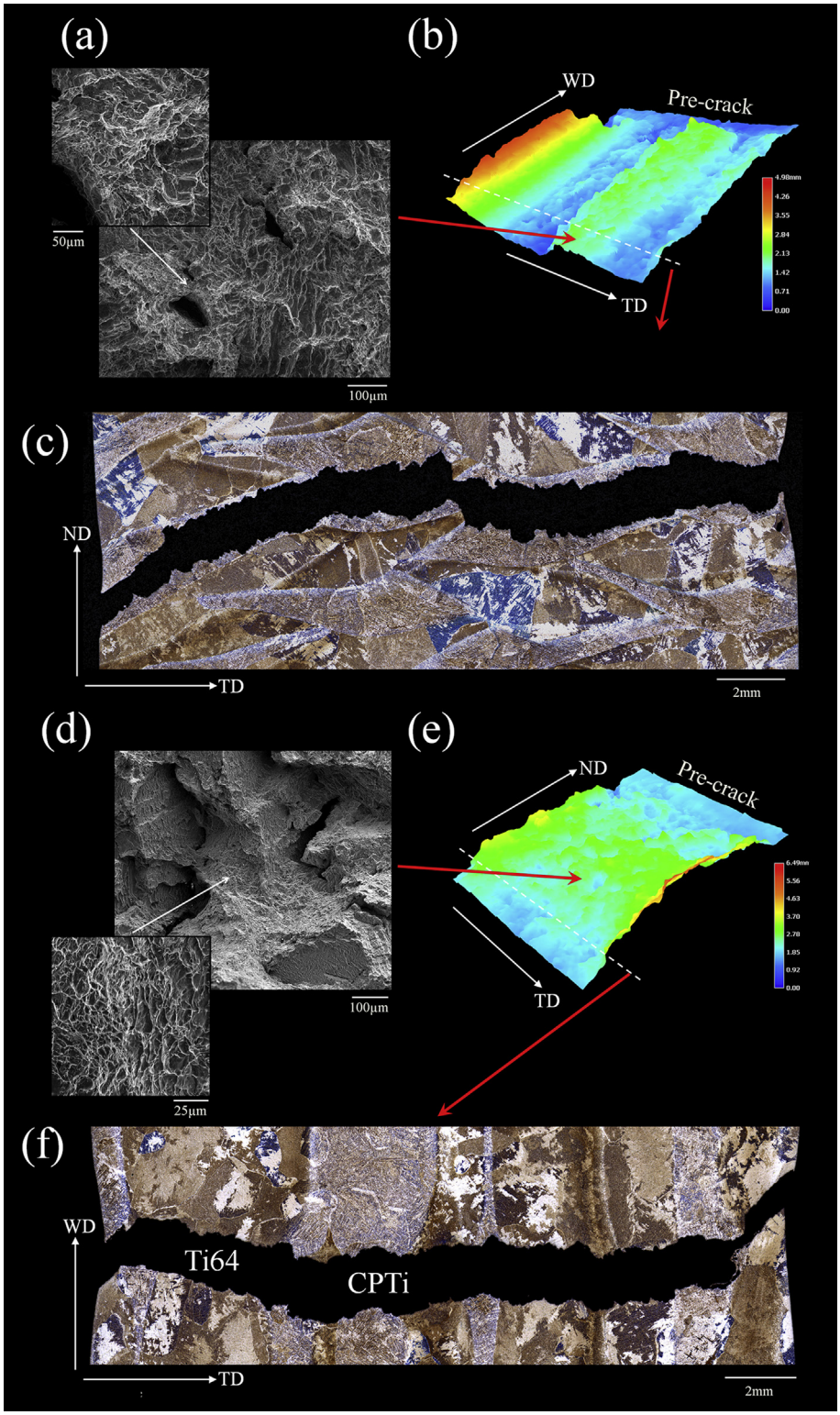

Fig. 11. Analysis of the fracture behaviour of the AAC-WAAM fracture toughness specimens: (a)–(c) the WD-ND sample, (d)–(f) the ND-WD sample showing: (a) and (d) SEM images of the fracture surfaces, (b) and (e) 3D reconstructions of the surface topography, and (c) and (f) optical micrographs of the crack seen in the two cross sections.

have on their microstructure, as well as to determine if their fracture behaviour could be positively influenced by developing an alternating microstructure.

4.1. Mixing and dilution

Taken together, the low resolution EDS data, hardness maps, and high-resolution quantified EPMA maps, show that extensive mixing took place between the dual-alloy wire feeds when they were alternately deposited in the WAAM process. This led to significant dilution

of the Ti64 and enrichment of the CPTi feedstock wires during their addition to the melt pool. In AM, as the process parameters are optimised to avoid lack of fusion defects when depositing alternating alloy tracks, a large amount of dilution is inevitable. Indeed, in most AM processes, the fraction of substrate re-melting (or track overlap) is in the range of 50–70% of the total melt pool volume [8,64]; and with similar deposition conditions to those used here, the average dilution of the added material by the substrate in the WAAM process is known to be approaching 70% [71]. With the simple alternating raster pattern used (see Fig. 1), previously deposited tracks produced with Ti64 and grade 2 CPTi wires will both be partially melted when the next track is deposited, with contributions to the re-melt volume from tracks both in the previous layer beneath the melt pool and from the neighbouring alternate track in the same added layer. Each alternate alloy track will have also been previously diluted within the melt pool when it was first deposited. After several layers have been added, a steady state will thus develop where the previously mixed solute-rich and solute-lean tracks are partially re-melted and alloyed with each new track. If the average composition of the feed wires is taken as the re-melted substrate composition (5.7 wt% Al and 3.7 wt% V for Ti64), and this is mixed with either CPTi or Ti64, to give the average compositions of the solute rich and solute lean regions (Ti-3.5Al-2.3 V and Ti-1.3Al-0.7 V) the average dilution can be estimated to be ~ 45% for the CPTi and ~ 75% for the Ti64 wire i.e. the ratio of re-melted substrate to wire melted in the melt pool was approximately 45:55 and 75:25 for the CPTi and Ti64 wires, respectively. This is also evident from the maps shown in Figs. 4c and 6, which revealed that the alloy rich regions have a larger volume fraction than the alloy lean matrix (~ 67% relative to 33%, calculated by image analysis). As constant welding process conditions were used to deposit each alloy, this result is, at face value, surprising as the melting point and latent heat of fusion of CPTi and Ti64 are similar [3,72]. Nevertheless, there are a number of additional factors that could have affected the different dilution ratios. Most significantly, the bead profile of each track depends on the surface tension and melt-pool viscosity, which would be expected to vary with composition, and thus affect the penetration into the previous layer relative to the extent of re-melting of the alternate neighbouring track.

However, higher resolution hardness mapping and composition analysis have shown that the actual composition ranges within the deposited material were restricted to two relatively narrow bands, corresponding to regions of diluted Ti64 and enriched grade 2 CPTi, the majority of which had a limited composition spread of 3–3.6 wt% Al and 2–2.6% V, and between 0.8 and 1.2 wt% for Al and 0.5–1% for V respectively. This can be confirmed from Fig. 12, where microhardness and Al EDS frequency distributions are compared using data taken from the large area maps in Figs. 4c and 6a. These graphs show that the majority of the data is concentrated in two peaks correlated to the regions of diluted Ti64 and enriched grade 2 CPTi, and demonstrates the importance of solid solution strengthening by Al in the dominant alpha phase in controlling the local yield strength [2,60]. In contrast, few regions have compositions or hardness values expected for the constituent pure wires and formed small isolated islands within the hardness/composition maps.

This bimodal composition behaviour was aided by effective mixing within the liquid phase (Figs. 7–8), with only small variations seen in composition measured in the solute-rich and solute-lean regions, due to stirring from buoyancy and Marangoni convection and liquid flow induced by arc forces [73–75]. Efficient mixing also resulted in a narrow ~ 70 μm thick boundary layer between each track. The thin boundary layer also suggests that there is insufficient time for solid-state interdiffusion to significantly homogenise the composition gradients achieved after solidification, due to the rapid thermal cycle in an AM process. The net result of the large dilution of each track, and high degree of liquid phase mixing, is thus an alloy-alloy composite material comprised of interlayered filaments of surprisingly regular bimodal composition. The alloy 'composite' deposited can thus be thought of as being comprised of two 'phases' of distinctly different composition, with each phase having a relatively uniform alloy content that is less extreme than that of the constituent feed wires, with a narrow boundary layer exhibiting a steep composition and microstructure gradient between each 'phase'.

4.2. β-Grain refinement

An interesting observation made in this work is that, compared to in conventional Ti64 WAAM builds which generally suffer from undesirable coarse columnar β-grain structures [6,24–27], the AAC-WAAM deposited material contained a refined, mixed grain structure comprised of much smaller columnar β grains, interspersed with a low fraction of isolated, finer, near-equiaxed grains (Fig. 5b and c). As similar deposition parameters were used to those typically adopted for depositing monolithic Ti64 WAAM material [1,6,31], this suggests that re-melting and solidification of a moving melt pool with an alternating composition can disrupt the development of the coarse, columnar β grains normally seen in WAAM deposits for metallurgical reasons.

The isolated equiaxed grains seen in Fig. 5 are highlighted in a magnified map in Fig. 13 and appear to have positions associated with the transition in composition between the solute-rich and solute-lean deposition tracks, which is also close to the position of the fusion boundary. In particular, the presence of equiaxed grains with non-< 001 > //ND fibre orientations (e.g. the blue grain in Fig. 13) indicates that limited re-nucleation is occurring ahead of the solidification front, which is sufficient to disrupt the continual epitaxial regrowth through multiple layers that is normally seen with WAAM of a monolithic Ti alloy. This supply of new nuclei will give rise to more limited columnar growth of favourably orientated grains with a < 001 > //ND fibre orientation before they are cut off by the presence of more new nuclei formed at the solidification front. Growth of more favourably orientated new gains will also leave behind less favourably orientated nuclei with random orientations, to become isolated equiaxed grains. This interpretation is consistent with Fig. 13, where in the EBSD data shown it can be seen that the orientations of the equiaxed island grains' < 001 > poles are all tilted greater than 20° away from the ~ < 001 > //ND alignment shown by their columnar neighbours.

Upon solidification during the WAAM process, β-grain nucleation can be promoted ahead of the solidification front by alloying Ti with certain elements that partition more strongly and cause a greater constitutional undercooling [25]. For example, this technique has been utilised recently using elements with low partition coefficients in Ti such as Si [39] and B [76]. However, the benefit of this method, without any accompanying inoculation [77], has been shown to be mainly to reduce the width of the columnar grains through increasing 'growth restriction' (Q factor [65,66]). Here, this mechanism is not relevant as we are simply diluting Ti64 and both Al and V already exhibit very low partitioning in Ti ($k \approx 1$ [65,66]). Alternative explanations are: i) a change in the β lattice parameter, caused by different compositions between the liquid and substrate, increases the barrier to nucleation and makes epitaxial nucleation less favourable; ii) diluting the liquid changes the melting point, leading to a melting point gradient in the chemical boundary layer creating greater undercooling; or iii) more dendrite fragmentation occurs. i) is a definite possibility, but alone is likely to be of limited effectiveness as the percentage change in lattice parameter from Al and V is relatively small [78]. With respect to ii), pure Ti is predicted to have a lower melting point than Ti64 by 35 °C (JMatPro calculation [68]) due to the presence of Al, which increases the melting point in the range 0–6 wt%. Even if dilution is taken into account, a difference in melt-pool substrate composition of ~ 3% Al will still lead to a significant melting point gradient at the fusion boundary of the order of 0.24 °C/μm. In comparison, dendrite fragmentation seems less likely, owing to the narrow mushy zone expected for Ti64, which will also decrease in width if it is further diluted [79,80]. Overall, it thus appears that a small increase in the energy

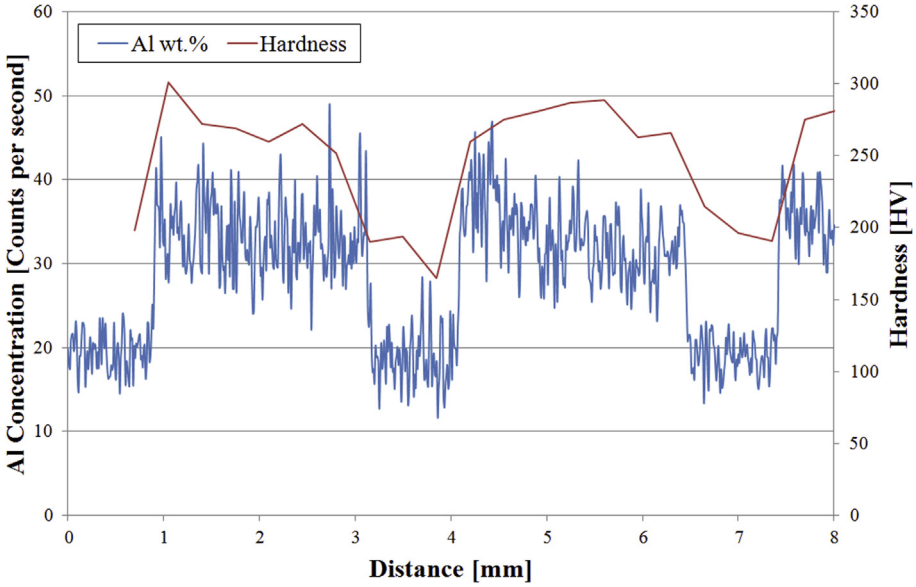

Fig. 12. Hardness and Al SEM-EDS line scans taken from the data in the large area maps in Figs. 4c and 6a, showing the change in hardness with respect to the Al solid-solution strengthening of each soft (Al lean) and hard (Al heavy) wire filament, due to the alternating Ti64 and CPTi deposits.

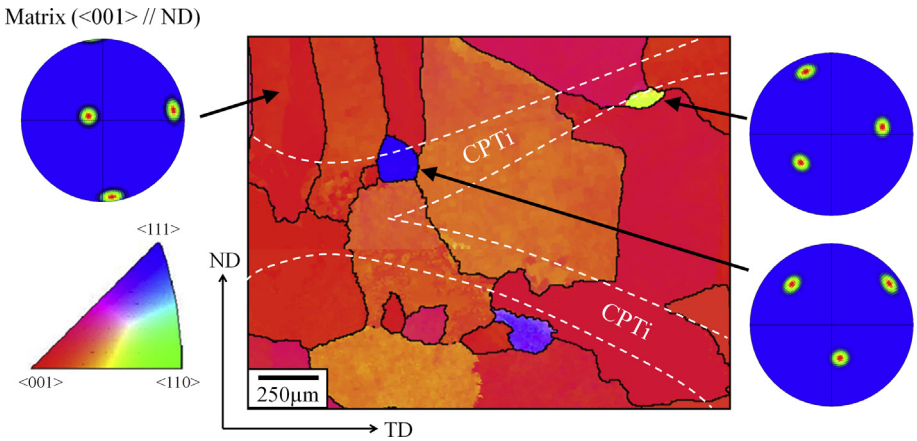

Fig. 13. Enlarged reconstructed β EBSD map with ND IPF colouring, showing fine equiaxed grains of non- < 001 > //ND fibre orientation associated with the transition in composition between solute rich and lean deposition tracks. The boundaries of the solute lean layers are indicated by the dashed lines.

barrier for epitaxial nucleation, combined with the promotion of melting point gradients at the fusion boundary, may be sufficient to promote rare new nucleation events at the solidification front which gives rise to this effect.

Finally, while we acknowledge that at this stage more work is required to elucidate the exact mechanism, the refinement of the grain structure reported above is an important practical result, owing to the undesirable technological impact of a coarse, columnar β−grain structure on the anisotropy and mechanical performance of Ti64 AM components [24,31,34].

4.3. Mechanical behaviour and potential for future exploitation

The tensile yield strength and UTS of the dual alloy composite material built by the WAAM process were generally lower than that of Ti64, and approximately midway between that of the two alloys from which it was produced. This is not that surprising given that the AAC material deposited was produced from constituent feedstock wires consisting of a weaker grade 2 CPTi mixed 50:50 with a stronger Ti64 material. In addition, it has now been established that the compositions of both alloys were substantially altered during the deposition process, leading to a material containing interlayered filaments, which were aligned in WD, comprised of a ~ 70% volume fraction of a harder alloy, with an approximate composition of Ti-3.5Al-2.3 V; alternating with a softer more dilute material with an average composition of Ti-1.3Al-0.7 V. Both of these constituent 'phases' were thus softer than that of the stronger Ti64 alloy from which the AAC was produced. Although significant microstructure variation was observed between the two constituent 'phases', including a larger α lamellar spacing in the alloy lean regions and a near-zero β content, the hardness variation could be directly correlated to the change in alloy content, which suggests the yield stress of each region was dominated by solid-solution strengthening of the dominant α phase (mainly by Al [2,60]). The opportunity therefore still exists to increase the strength of Ti64 by depositing in tandem with a richer alloy wire, or an alternative higher strength alloy, rather than using CPTi.

The AAC material also exhibited a double inflection yield behaviour in its tensile stress strain curves, which gave a higher yield stress in the loading direction parallel to the direction of alignment of the alternating tracks. This occurred simply because of the 'weak link principle', whereby yielding can occur more easily in the softer phase before strain hardening and load transfer to the stronger alloy leads to a rapid increase in flow stress. For example, it has been demonstrated recently by Pope et al. [52] that, when tensile tested, CPTi–Ti64 dissimilar welds

first yield and then fail in the weaker CPTi material with a lower elongation due to strain concentration. In addition, similar to fibre-reinforced composites, load transfer to the stronger alloy would also be expected to be more significant on loading parallel to the direction of track alignment (WD). However in the AAC material, the double inflection yield behaviour presented here would be affected by scale, and this effect would likely be smeared out should larger samples be tested. The elongation to failure was higher in the WD direction and consistent with that expected from a material in between Ti64 and grade 2 CPTi; whereas it was considerably poorer in the transverse direction because, when deformed normal to the layers, strain concentrated within the weaker 'phase', which in the WD-TD plane was interconnected through the sample thickness leading to premature necking. A similar behaviour is also commonly seen in transverse tensile tests performed across welded materials due to fusion zone, or HAZ softening (e.g. Ref. [81]).

The yield-stress asymmetry found between the ND and WD loading was similar to that seen in monolithic Ti64 WAAM test results. In the Ti64 deposits, this is caused by the α transformation texture inherited from the strong β solidification texture [26], whereas in the AAC material it arises from the geometry-related different efficiencies of load transfer between the soft and hard materials, relative to their alignment with respect to the loading direction. In contrast, the asymmetry in strain to failure to between ND and WD loading was found to be reversed relative to that seen in Ti64 WAAM [31,32]. This difference in behaviour occurs because earlier tensile failure in WD in monolithic Ti64 deposits is caused by plastic heterogeneity generated by harder α texture regions inherited from the very coarse columnar β grains present, which are aligned transverse to the tensile axis in this loading direction, and final fracture is influenced by grain boundary α on the parallel transverse β boundaries in such samples [24]. Variation in the coarse β − grain structure and grain orientations also gives rise to the larger scatter seen in this loading direction in the elongation to failure in conventional WAAM material [24,31]. In comparison, in the alloy composite material, ductility in WD was higher than in ND because of premature localisation of plasticity and necking in the weaker solute-lean phase in the WD test orientation. Less scatter is also seen in the test data due to the refined β grain size and regular nature of the alternate alloy deposition tracks.

Although there is evidence of the stronger 'phase' constraining the weaker material regions in the AAC tensile samples (Fig. 10a), because of the relatively coarse length scale of each alternating phase (e.g. 1 – 2 mm thick filaments) this does not lead to a significant property advantage over and above that of a chemically homogenous alloy, and it has the disadvantage of promoting greater plastic heterogeneity in the transverse loading situation. Such a coarse length scale composite system can also not take advantage of mechanisms that can be exploited to inhibit dislocation-facilitated plasticity and increase strength at the nanoscale (which are beneficial in deformation processed metal–metal composites that have layer thicknesses as small as 10 nm [49]). This alloy combination also cannot gain from elastic shielding effects seen in conventional composite materials that have different stiffness constituents [49]. Therefore, using WAAM technology to combine strong and weak alloys at this relatively coarse length scale to engineer simple tensile properties does not have many clear advantages. In addition, promoting local plastic yielding by incorporating a soft interconnected phase into a material with too large a scale is unlikely to be beneficial for high cycle fatigue initiation life.

The main mechanical-performance advantages of printing a composite formed from alternate alloys at this length scale are, therefore, most likely to reside in artificial control of the fracture propagation path and increasing its tortuosity, which could potentially be exploited to control crack paths in long fatigue crack growth where closure dominates crack growth rates. In this initial study, the fracture toughness was only slightly improved relative to that of monolithic Ti64 test results, but there was clear evidence that the crack did follow the interconnected weaker dilute phase in the WD-ND sample test results, which increased the macroscopic roughness of the fracture surface. However, the simple aligned arrangement of the alternating alloy tracks deposited in this preliminary study did not maximise the potential for increasing crack deflection and fracture surface area, and this could be better exploited by using a different deposition strategy. For example, the traverse direction could have been rotated 90^0 in alternate layers to more dramatically change the crack path.

5. Conclusions

A first stage study has been performed to investigate the potential for exploiting high deposition rate AM techniques to print dual alloy microstructures. WAAM deposition, using alternating wires of CPTi and Ti64, has been shown to be effective in generating an 'Alloy-Alloy' Composite (AAC) material, comprised of regular, interlinked, aligned filaments formed from alloys of alternating composition. This work has also revealed the unanticipated novel effect that printing alternate alloy compositions can cause significant β-grain refinement and α texture weakening, relative to that seen in a conventional monolithic Ti WAAM product. This latter effect is of important practical significance owing to the undesirable impact of a coarse, columnar β − grain structure on the anisotropy and mechanical performance of Ti64 AM components.

As AM process parameters are optimised to avoid lack of fusion defects, a large level of melt pool dilution (60–70%) occurred during deposition, which resulted in a significant composition change in each deposited track relative to that of the respective feed wire used. A high degree of liquid phase mixing was also confirmed, promoted by the melt pool hydrodynamics, driven by the strong Marangoni convection effects acting in small moving melt pools. Thus, when alternate alloys were deposited, an AAC material was produced comprised of a surprisingly regular bimodal composition, containing two 'phases' of distinctly different alloy content, with each 'phase' having a relatively uniform composition range that was less extreme than that of the constituent feed wires. In addition, only a relatively narrow boundary layer (< 100 μm) exhibiting a composition and microstructure gradient was found to be produced between each 'phase'.

The tensile yield strength and UTS of the dual alloy composite material, printed by the WAAM process, were generally lower than that of Ti64 and approximately midway between that of the two alloys from which it was produced. The AAC material also exhibited a double-inflection yield behaviour in its stress-strain curves, and had a higher yield stress in the loading direction parallel to the direction of alignment of the alternating tracks. When tested perpendicular to the layers, strain localisation in the weaker lean alloy (CPTi) resulted in premature necking and an overall elongation to failure 50% lower than when loaded parallel to the alternating alloy deposition tracks. Overall, because of the relatively coarse length scale of each 'phase' in the AAC (e.g. 1 – 2 mm thick filaments), a significant property advantage was not seen in tensile tests over and above that of a chemically homogenous material, and the AAC had the disadvantage of promoting greater plastic heterogeneity in transverse loading.

The main mechanical performance advantage of printing a composite formed from alternate alloys at this length scale is, therefore, likely to reside in increasing the tortuosity of the fracture path. In this initial study, the fracture toughness was improved relative to that of monolithic Ti64 test results, and there was clear evidence that the crack followed the weaker phase in WD-ND sample test results, which increased the macroscopic roughness of the fracture surface. However, the simple aligned arrangement of the alternating alloy tracks in the materials investigated did not maximise the potential for increasing the crack surface area or crack deflection, and in the future this could be better exploited by using an improved deposition strategy.

Finally, the AAC WAAM deposited material was found to have a refined, mixed grain structure comprised of much smaller, columnar β-grains than seen in a conventional Ti64 build, containing some isolated, finer, equiaxed grains. The isolated and equiaxed grains had positions

associated with the transition in composition between solute-rich and solute-lean deposition tracks, suggesting that composition gradients introduced by dual-alloy printing were promoting limited nucleation ahead of the solidification front, and thereby disrupting the epitaxial columnar growth that is normally seen in Ti WAAM deposits. It is postulated that this effect may arise from a small increase in the energy barrier for epitaxial nucleation, associated with a lattice parameter change, combined with the promotion of a melting point gradient at the fusion boundary caused by the steep composition gradients generated by alternate alloy deposition, which together may be sufficient to promote new nucleation events at the solidification front.

Data availability

The raw and processed data required to reproduce these findings cannot be shared at this time due to technical or time limitations.

Acknowledgements

The authors are appreciative of the EPSRC grants (LightForm - EP/R001715/1; NEWAM – EP/R027218/1) and Innovate UK (Open Architecture Additive Manufacturing, OAAM) for supporting aspects of this research. Professor P.B. Prangnell is grateful to the Royal Academy of Engineering, UK, and Airbus for financial support through the Airbus-University of Manchester Centre for Metallurgical Excellence.

Appendix A. Supplementary data

Supplementary data to this article can be found online at https://doi.org/10.1016/j.msea.2019.138289.

References

[1] X. Zhang, F. Martina, J. Ding, X. Wang, S.W. Williams, Fracture toughness and fatigue crack growth rate properties in wire + arc additive manufactured Ti-6Al-4V, Fatigue Fract. Eng. Mater. Struct. 40 (5) (2017) 790–803.
[2] G. Lütjering, J.C. Williams, Titanium, Springer, 2007.
[3] ASM International, Materials Properties Handbook: Titanium Alloys, Materials Park, OH., 1994.
[4] F. Martina, J. Mehnen, S.W. Williams, P.A. Colegrove, F. Wang, Investigation of the benefits of plasma deposition for the additive layer manufacture of Ti-6Al-4V, J. Mater. Process. Technol. 212 (6) (2012) 1377–1386.
[5] T. Duda, L.V. Raghavan, 3D metal printing technology, 49 (29) (2016) 103–110 IFAC-PapersOnLine.
[6] F. Martina, P.A. Colegrove, S.W. Williams, J. Meyer, Microstructure of interpass rolled wire + arc additive manufacturing Ti-6Al-4V components, Metall. Mater. Trans. A Phys. Metall. Mater. Sci. 46 (12) (2015) 6103–6118.
[7] A.C.M. Bekker, J.C. Verlinden, Life cycle assessment of wire + arc additive manufacturing compared to green sand casting and CNC milling in stainless steel, J. Clean. Prod. 177 (2018) 438–447.
[8] S. Ríos, P.A. Colegrove, F. Martina, S.W. Williams, Analytical process model for wire + arc additive manufacturing, Addit. Manuf. 21 (April) (2018) 651–657.
[9] S.W. Williams, F. Martina, A.C. Addison, J. Ding, G. Pardal, P.A. Colegrove, Wire + arc additive manufacturing, Mater. Sci. Technol. 32 (7) (2015) 641–647.
[10] P.W. Fuerschbach, G.A. Knorovsky, A study of melting efficiency in plasma-arc and gas tungsten arc-welding, Weld. J. 70 (11) (1991) 287–297.
[11] N. Stenbacka, On arc efficiency in gas tungsten arc welding, 18 (4) (2013) 380–390 Soldag. Inspeção.
[12] J.S. Zuback, T.A. Palmer, T. DebRoy, Additive manufacturing of functionally graded transition joints between ferritic and austenitic alloys, J. Alloy. Comp. 770 (2019) 995–1003.
[13] D.C. Hofmann, et al., Developing gradient metal alloys through radial deposition additive manufacturing, Sci. Rep. 4 (2014).
[14] C. Schneider-Maunoury, L. Weiss, D. Boisselier, P. Laheurte, Crystallographic analysis of functionally graded titanium-molybdenum alloys with DED-CLAD® process, Procedia CIRP 74 (2018) 180–183.
[15] C. Schneider-Maunoury, L. Weiss, O. Perroud, D. Joguet, D. Boisselier, P. Laheurte, An application of differential injection to fabricate functionally graded Ti-Nb alloys using DED-CLAD ® process, J. Mater. Process. Technol. 268 (January) (2019) 171–180.
[16] B. Onuike, A. Bandyopadhyay, Additive manufacturing of Inconel 718 – Ti6Al4V bimetallic structures, Addit. Manuf. 22 (June) (2018) 844–851.
[17] B. Vamsi Krishna, W. Xue, S. Bose, A. Bandyopadhyay, Functionally graded Co-Cr-Mo coating on Ti-6Al-4V alloy structures, Acta Biomater. 4 (3) (2008) 697–706.
[18] R. Banerjee, P.C. Collins, D. Bhattacharyya, S. Banerjee, H.L. Fraser, Microstructural evolution in laser deposited compositionally graded α/β titanium-vanadium alloys, Acta Mater. 51 (11) (2003) 3277–3292.
[19] J. Wang, et al., Characterization of wire arc additively manufactured titanium aluminide functionally graded material: microstructure, mechanical properties and oxidation behaviour, Mater. Sci. Eng. A 734 (May) (2018) 110–119.
[20] A. Ho, H. Zhao, J.W. Fellowes, F. Martina, A.E. Davis, P.B. Prangnell, On the origin of microstructural banding in Ti-6Al4V wire-arc based high deposition rate additive manufacturing, Acta Mater. 166 (2019).
[21] E. Hernández-Nava, P. Mahoney, C.J. Smith, J. Donoghue, I. Todd, S. Tammas-Williams, Additive manufacturing titanium components with isotropic or graded properties by hybrid electron beam melting/hot isostatic pressing powder processing, Sci. Rep. 9 (1) (2019) 1–11.
[22] Y. Wang, H.M. Wang, Wear resistance of laser clad Ti 2 Ni 3 Si reinforced intermetallic composite coatings on titanium alloy, Appl. Surf. Sci. 229 (1–4) (2004) 81–86.
[23] B. Baufeld, E. Brandl, O. Van Der Biest, Wire based additive layer manufacturing: comparison of microstructure and mechanical properties of Ti-6Al-4V components fabricated by laser-beam deposition and shaped metal deposition, J. Mater. Process. Technol. 211 (6) (2011) 1146–1158.
[24] P. Åkerfeldt, M.L. Antti, R. Pederson, Influence of microstructure on mechanical properties of laser metal wire-deposited Ti-6Al-4V, Mater. Sci. Eng. A 674 (2016) 428–437.
[25] T. DebRoy, et al., "Additive manufacturing of metallic components – process , structure and properties, Prog. Mater. Sci. 92 (2018) 112–224.
[26] J. Donoghue, A.A. Antonysamy, F. Martina, P.A. Colegrove, S.W. Williams, P.B. Prangnell, The effectiveness of combining rolling deformation with Wire-Arc Additive Manufacture on β-grain refinement and texture modification in Ti-6Al-4V, Mater. Char. 114 (2016) 103–114.
[27] A.A. Antonysamy, J. Meyer, P.B. Prangnell, Effect of build geometry on the β-grain structure and texture in additive manufacture of Ti6Al4V by selective electron beam melting, Mater. Char. 84 (2013) 153–168.
[28] P.A. Kobryn, S.L. Semiatin, Microstructure and texture evolution during solidification processing of Ti-6A1-4V, J. Mater. Process. Technol. 135 (2–3 SPEC) (2003) 330–339.
[29] A.A. Antonysamy, P.B. Prangnell, J. Meyer, Effect of wall thickness transitions on texture and grain structure in additive layer manufacture (ALM) of Ti-6Al-4V, Mater. Sci. Forum 706 (709) (2012) 205–210.
[30] S.S. Al-Bermani, M.L. Blackmore, W. Zhang, I. Todd, The origin of microstructural diversity, texture, and mechanical properties in electron beam melted Ti-6Al-4V, Metall. Mater. Trans. A Phys. Metall. Mater. Sci. 41 (13) (2010) 3422–3434.
[31] F. Martina, S.W. Williams, P.A. Colegrove, Improved microstructure and increased mechanical properties of additive manufacture produced Ti-6Al-4V by interpass cold rolling, SFF Symp (2013) 490–496.
[32] T. Vilaro, C. Colin, J.D. Bartout, As-fabricated and heat-treated microstructures of the Ti-6Al-4V alloy processed by selective laser melting, Metall. Mater. Trans. A Phys. Metall. Mater. Sci. 42 (10) (2011) 3190–3199.
[33] I. Bantounas, D. Dye, T.C. Lindley, The role of microtexture on the faceted fracture morphology in Ti-6Al-4V subjected to high-cycle fatigue, Acta Mater. 58 (11) (2010) 3908–3918.
[34] F. Wang, S.W. Williams, P.A. Colegrove, A.A. Antonysamy, Microstructure and mechanical properties of wire and arc additive manufactured Ti-6Al-4V, Metall. Mater. Trans. A Phys. Metall. Mater. Sci. 44 (2) (2013) 968–977.
[35] H. Zhao, A. Ho, A.E. Davis, A.A. Antonysamy, P.B. Prangnell, Automated image mapping and quantification of microstructure heterogeneity in additive manufactured Ti6Al4V, Mater. Char. 147 (July 2018) (2019) 131–145.
[36] I. Smirnov, A. Polyakov, Y. Sudenkov, Strength and fracture of ultrafine-grained titanium Grade 4, Procedia Struct. Integr. 6 (2017) 196–200.
[37] I. Sabirov, R.Z. Valiev, I.P. Semenova, R. Pippan, Effect of equal channel angular pressing on the fracture behavior of commercially pure titanium, Metall. Mater. Trans. A Phys. Metall. Mater. Sci. 41 (3) (2010) 727–733.
[38] P. Edwards, M. Ramulu, Effect of build direction on the fracture toughness and fatigue crack growth in selective laser melted Ti-6Al-4-‰V, Fatigue Fract. Eng. Mater. Struct. 38 (10) (2015) 1228–1236.
[39] S. Mereddy, M.J. Bermingham, D.H. StJohn, M.S. Dargusch, Grain refinement of wire arc additively manufactured titanium by the addition of silicon, J. Alloy. Comp. 695 (2017) 2097–2103.
[40] K. Yamanaka, W. Saito, M. Mori, H. Matsumoto, A. Chiba, Preparation of weak-textured commercially pure titanium by electron beam melting, Addit. Manuf. 8 (2015) 105–109.
[41] A. Barbas, A.S. Bonnet, P. Lipinski, R. Pesci, G. Dubois, Development and mechanical characterization of porous titanium bone substitutes, J. Mech. Behav. Biomed. Mater. 9 (2012) 34–44.
[42] H. Attar, M. Calin, L.C. Zhang, S. Scudino, J. Eckert, Manufacture by selective laser melting and mechanical behavior of commercially pure titanium, Mater. Sci. Eng. A 593 (2014) 170–177.
[43] S.A. David, J.M. Vitek, Correlation between solidification parameters and weld microstructures, Int. Mater. Rev. 34 (5) (1989) 213–244.
[44] F. Fomin, M. Froend, V. Ventzke, P. Alvarez, S. Bauer, N. Kashaev, Metallurgical aspects of joining commercially pure titanium to Ti-6Al-4V alloy in a T-joint configuration by laser beam welding, Int. J. Adv. Manuf. Technol. 97 (5–8) (2018) 2019–2031.
[45] L. Weiss, J. Zollinger, P. Sallamand, E. Cicala, A. Mathieu, E. Fleury, Mechanical properties and microstructural study of homogeneous and heterogeneous laser welds in α, β, and α + β titanium alloys, Weld. World 63 (1) (2019) 53–62.
[46] A. Thiriet, C. Schneider-Maunoury, P. Laheurte, D. Boisselier, L. Weiss, Multiscale study of different types of interface of a buffer material in powder-based directed

energy deposition: example of Ti6Al4V/Ti6Al4V - Mo/Mo - Inconel 718, Addit. Manuf. 27 (September 2018) (2019) 118–130.
[47] A. Bandyopadhyay, B. Heer, Additive manufacturing of multi-material structures, Mater. Sci. Eng. R Rep. 129 (April) (2018) 1–16.
[48] B. Onuike, B. Heer, A. Bandyopadhyay, Additive manufacturing of Inconel 718—copper alloy bimetallic structure using laser engineered net shaping (LENS^{TM}), Addit. Manuf. 21 (February) (2018) 133–140.
[49] A.M. Russell, L.S. Chumbley, Y. Tian, Deformation-processed metal-metal composites, Adv. Eng. Mater. 2 (1–2) (2000) 11–22.
[50] C.H. Young, H.K.D.H. Bhadeshia, Strength of mixtures of bainite and martensite, Mater. Sci. Technol. 10 (1994) 209–214.
[51] P.C. Collins, R. Banerjee, S. Banerjee, H.L. Fraser, Laser deposition of compositionally graded titanium-vanadium and titanium-molybdenum alloys, Mater. Sci. Eng. A 352 (1–2) (2003) 118–128.
[52] J.J. Pope, E.L. Calvert, N.S. Weston, M. Jackson, FAST-DB: a novel solid-state approach for diffusion bonding dissimilar titanium alloy powders for next generation critical components, J. Mater. Process. Technol. 269 (June 2018) (2019) 200–207.
[53] ASTM Standard E399, Standard test method for linear-elastic plane-strain fracture toughness KIc of metallic materials, *ASTM International*, Pennsylvania, US, 2013.
[54] C.A. Schneider, W.S. Rasband, K.W. Eliceiri, NIH Image to ImageJ: 25 years of image analysis, Nat. Methods 9 (7) (2012) 671–675.
[55] P.S. Davies, An Investigation of Microstructure and Texture Evolution in the Near-α Titanium Alloy Timetal 834, University of Sheffield, 2009.
[56] P.S. Davies, B.P. Wynne, W.M. Rainforth, M.J. Thomas, P.L. Threadgill, Development of microstructure and crystallographic texture during stationary shoulder friction stir welding of Ti-6Al-4V, Metall. Mater. Trans. A Phys. Metall. Mater. Sci. 42 (8) (2011) 2278–2289.
[57] M. Humbert, N. Gey, The calculation of a parent grain orientation from inherited variants for approximate (b.c.c.-h.c.p.) orientation relations, J. Appl. Crystallogr. 35 (4) (2002) 401–405.
[58] N. Gey, M. Humbert, Specific analysis of EBSD data to study the texture inheritance due to the β→α phase transformation, J. Mater. Sci. 38 (6) (2003) 1289–1294.
[59] H. Attar, S. Ehtemam-Haghighi, D. Kent, M.S. Dargusch, Recent developments and opportunities in additive manufacturing of titanium-based matrix composites: a review, Int. J. Mach. Tool Manuf. 133 (June) (2018) 85–102.
[60] A. Fitzner, et al., The effect of aluminium on twinning in binary alpha-titanium, Acta Mater. 103 (2016) 341–351.
[61] D. Hull, T.W. Clyne, An Introduction to Composite Materials, second ed., Cambridge University Press, Cambridge, UK, 2006.
[62] J. Wang, et al., Grain morphology evolution and texture characterization of wire and arc additive manufactured Ti-6Al-4V, J. Alloy. Comp. 768 (2018) 97–113.
[63] E. Brandl, B. Baufeld, C. Leyens, R. Gault, Additive manufactured Ti-6A1-4V using welding wire: comparison of laser and arc beam deposition and evaluation with respect to aerospace material specifications, Phys. Procedia 5 (2) (2010) 595–606.
[64] X. Bai, et al., Numerical analysis of heat transfer and fluid flow in multilayer deposition of PAW-based wire and arc additive manufacturing, Int. J. Heat Mass Transf. 124 (2018) 504–516.
[65] M.J. Bermingham, S.D. McDonald, M.S. Dargusch, D.H. StJohn, Grain-refinement mechanisms in titanium alloys, J. Mater. Res. 23 (1) (2008) 97–104.
[66] T. Lyman, Atlas of Microstructures of Industrial Alloys, American Society for Metals, 1972.
[67] W.F. Gale, T.C. Totemeier (Eds.), Smithells Metals Reference Book, eighth ed., Elsevier, Oxford, 2004.
[68] N. Saunders, Z. Guo, X. Li, A.P. Miodownik, J.P. Schillé, Using JMatPro to model materials properties and behavior, JOM (J. Occup. Med.) 55 (12) (2003) 60–65.
[69] J. Donoghue, A. Gholinia, J. Quinta da Fonseca, P.B. Prangnell, In-situ high temperature EBSD analysis of the effect of a deformation step on the alpha to beta transition in additive manufactured Ti-6Al-4V, TMS Titan. (2015) 1283–1288.
[70] H. Galarraga, R.J. Warren, D.A. Lados, R.R. Dehoff, M.M. Kirka, Fatigue crack growth mechanisms at the microstructure scale in as-fabricated and heat treated Ti-6Al-4V ELI manufactured by electron beam melting (EBM), Eng. Fract. Mech. 176 (2017) 263–280.
[71] A. Caballero, Dilution Study Ti-6Al-4V LAMP Project, (2018).
[72] J.L. McClure, A. Cezairliyan, Measurement of the heat of fusion of titanium and a titanium alloy (90Ti-6Al-4V) by a microsecond-resolution transient technique, Int. J. Thermophys. 13 (1) (1992) 75–81.
[73] K. Weman, Welding Processes Handbook, second ed., Woodhead Publishing Limited, Cambridge, UK, 2012.
[74] S. Lu, H. Fujii, K. Nogi, Marangoni convection and weld shape variations in Ar-O2 and Ar-CO2 shielded GTA welding, Mater. Sci. Eng. A 380 (1) (2004) 290–297.
[75] S. Lu, H. Fujii, H. Sugiyama, M. Tanaka, K. Nogi, Weld penetration and Marangoni convection with oxide fluxes in GTA welding, Mater. Trans. 43 (11) (2005) 2926–2931.
[76] M.J. Bermingham, D. Kent, H. Zhan, D.H. Stjohn, M.S. Dargusch, Controlling the microstructure and properties of wire arc additive manufactured Ti-6Al-4V with trace boron additions, Acta Mater. 91 (2015) 289–303.
[77] M.J. Bermingham, D.H. StJohn, J. Krynen, S. Tedman-Jones, M.S. Dargusch, Promoting the columnar to equiaxed transition and grain refinement of titanium alloys during additive manufacturing, Acta Mater. 168 (2019) 261–274.
[78] J.R. Kennedy, Development of a New Generation of Inoculants for Ti-Al Alloys, Université de Lorraine, 2018.
[79] M. Boivineau, et al., Thermophysical properties of solid and liquid Ti-6Al-4V (TA6V) alloy, Int. J. Thermophys. 27 (2) (2006) 507–529.
[80] D.A. Porter, K.E. Easterling, Phase Transformations in Metals and Alloys 3 (1992).
[81] H. Wu, Y.C. Chen, D. Strong, P. Prangnell, Stationary shoulder FSW for joining high strength aluminum alloys, J. Mater. Process. Technol. 221 (2015) 187–196.